Rock Mechanics Bulletin 4 (2025) 100155

Contents lists available at ScienceDirect

Rock Mechanics Bulletin

journal homepage: www.keaipublishing.com/en/journals/rock-mechanics-bulletin

Full Length Article

Dynamic evolution of reservoir permeability and deformation in geothermal battery energy storage using abandoned mines

Yanting Liu [a,b], Yuan Liang [c], Yueqiang Ma [a,b,*], Jingyi Liu [b], Derek Elsworth [d], Quan Gan [a,b,**]

[a] State Key Laboratory of Coal Mine Disaster Dynamics and Control, Chongqing University, Chongqing, 400044, China
[b] School of Resources and Safety Engineering, Chongqing University, Chongqing, 400044, China
[c] State Key Laboratory of Deep Coal Mining & Environment Protection, Huainan Mining Group Co., Ltd., Huainan, 232001, China
[d] Department of Energy and Mineral Engineering & Geosciences, EMS Energy Institute and G3 Center, Pennsylvania State University, University Park, PA, USA

ARTICLE INFO

Keywords:
Energy storage
Abandoned mines
Permeability evolution
Temperature sensibility
Thermal poroelasticity

ABSTRACT

Retasking existing subsurface abandoned mines as infrastructure for solar energy storage could be a feasible approach in overcoming the low thermal gradient present in shallow formations. In this work, the potential for thermal storage in the high permeability goaf of abandoned mines through diurnal cyclic injection-then-extraction using coupled thermo-hydro-mechanical modeling was explored by coupling FLAC^{3D} with TOUGH2. The temperature sensibility of reservoir during 30 days of cyclic injection-then-production was examined at various injection temperatures (ranging from 50 °C to 250 °C) and rates (ranging from 1 kg/s to 10 kg/s) and for representative reservoir physical and thermal properties, including variable thermal expansion coefficients. The simulation results reveal that: The principal mechanisms driving reservoir deformation result from the combined influence of thermal poroelastic and thermal effects. With the change of reservoir temperature, the reservoir is perturbed by pressure and thermal stresses causing permeability evolution. Permeability reduces ~10% for a maximum injection temperature of 250 °C – although effects are reduced the lower injection temperatures. The pore pressure fluctuations for an injection rate of 10 kg/s is ~6.5 times that for a rate of 1 kg/s. The pressure perturbation of the reservoir during the injection process decreases with the injection rate, and the reservoir is relatively more stable. When the thermal stress becomes predominant, the reservoir volume expands. Uplift displacements 220 m above the hot injection well are trivial an of the order of ~1.5 mm at a mean temperature of 163 °C.

1. Introduction

There are 12,000 abandoned mines in China (2020) with this number expected to grow to 15,000 by 2030 (Pu et al., 2022). To achieve efficient and reasonable secondary utilization in abandoned mines, China has actively explored and studied technologies such as compressed air energy storage (Bartela et al., 2022) and pumped energy storage (Koohi-Fayegh and Rosen, 2020) to address the intermittency problem of renewables. However, one-third of mines in China are flooded (Pu et al., 2022) with it more expensive to retrofit and operate such mines. One such option for utilizing such mining infrastructure is in accessing the geothermal resource present in mines, such as for geothermal energy recovery or as a "geothermal battery"(Green et al., 2021). A full-scale heat injection test in the low-temperature Illinois basin (USA) demonstrated the feasibility of such a geothermal battery energy storage system (Jello et al., 2022). The combination of a "geothermal battery" with abandoned mine infrastructure and space and accommodating local conditions is a pioneering "post-mining" technology (Ping et al., 2020) which potentially solves the problem of low utilization of solar energy due to the limitations of energy storage technology and thus enhances the efficiency of renewable energy utilization and contributes by driving a national energy transition.

Operation of any energy storage system in the subsurface impacts the dynamic evolution of temperature, permeability and porosity in the system. Injecting or extracting fluids from in and around subsurface mines and reservoirs disrupts the initial stress equilibrium, inducing variations in rock pore volume and fluid flow pathways as effective stresses change (Shao et al., 2020), which in turn cause changes in rock

* Corresponding author. State Key Laboratory of Coal Mine Disaster Dynamics and Control, Chongqing University, Chongqing, 400044, China.
** Corresponding author. State Key Laboratory of Coal Mine Disaster Dynamics and Control, Chongqing University, Chongqing, 400044, China.
E-mail addresses: mayq@cqu.edu.cn (Y. Ma), quan.gan@cqu.edu.cn (Q. Gan).

https://doi.org/10.1016/j.rockmb.2024.100155
Received 14 June 2024; Received in revised form 11 August 2024; Accepted 1 September 2024
Available online 14 September 2024

permeability. It is crucial to have insight into the reservoir mechanical response and the evolution of permeability for assessing the safety and service life of such energy storage systems during fluid injection and production (Gan et al., 2020). In addition to the fluid-mechanical field, thermal energy storage requires that the influence of thermal-mechanical coupling is also considered. Our understanding of THM coupling is well advanced and based on seepage experiments with rocks subjected to high-temperature treatments (from ambient to 800 °C) (Liu et al., 2020). Such studies examine the impact of temperature on the physical response of the rock mass (Yang et al., 2017), reveal the relationship between thermal damage and permeability evolution (Xu et al., 2023; Zhang and Zhao, 2023), establish empirical relationships between rock temperature and physical-mechanical properties (Wu et al., 2022), develop theoretical models correlating rock permeability with temperature and pressure (Becattini et al., 2017; Rosenbrand et al., 2015; Wang et al., 2023) under thermal poroelastic theory (Siratovich et al., 2015). Fracture permeability during geothermal exploitation depends on pore pressures (Guo et al., 2022), and effective stresses as during hydrocarbon recovery (Kozhevnikov et al., 2021), with transformations in permeability and recovery ratio during coal seam gas extraction (Fang et al., 2023). From these studies, the evolution of permeability is related to the effective stress within the reservoir and ultimately affects the recovery ratio of the system.

Some scholars have already investigated the permeability anisotropy (Panja et al., 2021a) and heterogeneity (Panja et al., 2021a) on the temperature and pressure distribution of the energy storage system, as well as the effects of reservoir porosity, thickness, thermal conductivity and injection rate on the system performance (Josiane et al., 2023). However, understanding the spatial and temporal evolution of reservoir permeability and deformation during the cyclic injection-extraction process is absent. Establishing the dynamic evolution of permeability over time and space at prototype engineering scale is necessary to optimize geothermal battery system performance. So the following establishes a 3D model of a geothermal battery energy storage system The dynamic evolution of reservoir permeability and porosity are followed while conducting a 30 days cyclic injection and extraction schedule, as a response to changes in injection-extraction temperature or rates throughout the cyclic period under the conditions of THM coupling. The reservoir deformation and changes in overburden/underburden displacement are monitored, the pressure disturbances generated by injection and extraction and predict the impact of subsurface deformation during the energy storage process.

2. Methodology and constitutive model

Detailed descriptions of the governing equations and constitutive models for permeability-porosity evolution in fractured media have been provided (Hu et al., 2018).

2.1. Governing equation

Mass and energy are conserved during fluid flow, with the integral form of the governing equations defined as (Pruess, 2004),

$$\frac{\mathrm{d}}{dt}\int_{V_n} M dV_n = \int_{\Gamma_n} F \cdot n d\Gamma_n + \int_{V_n} q dV_n \tag{1}$$

where M represents the unit volume mass of a specific fluid, V_n refers to any subdomain of the studied flow system bounded by the closed surface V_n, F represents mass flux, q denotes sinks or sources, n represents the normal vector to the surface element $d\Gamma_n$ pointing towards V_n, This equation signifies that the rate of change of mass in a specific volume V_n is equal to the net inflow across the entire surface of volume V_n including the inflow of fluid mass from sinks and sources.

The constitutive relations governing the equilibrium state of stress and strain, including the influence of thermal stress are defined as,

$$Gu_{i,jj} + \frac{G}{1-2\upsilon}u_{j,ji} - \alpha_B p_i - \alpha_T K T_i + F_i = 0 \tag{2}$$

where G is the shear modulus, Pa, u is the displacement, m; ν is the Poisson ratio; α_B is the Biot coefficient, p is the pore pressure, Pa, α_T represents the thermal expansion coefficient, $^{\circ}C^{-1}$, T is the temperature, °C, K is the rock bulk modulus, Pa, and F_i is the body force, N/m.

According to Duhamel-Neumann theory, a porous medium subjected to heating will generate internal thermal stresses as (Blanco Martín et al., 2015),

$$\sigma_{ij}^{corr} = \sigma_{ij} - \alpha \Delta P \delta_{ij} - 3\alpha_T K \Delta T \delta_{ij} \tag{3}$$

where σ_{ij} represents the total stress tensor, Pa, σ_{ij}^{corr} is the corrected tensor, Pa, δ_{ij} is the Kronecker delta, α is the Biot coefficient, ΔP is the pore pressure change, Pa, α_T represents the thermal expansion coefficient, $^{\circ}C^{-1}$, K is the rock bulk modulus, Pa, ΔT is the temperature change, °C.

The change in stress field results in mechanical deformation of the reservoir with rock porosity changing accordingly. The change in porosity during this heating process may be followed as (Davies and Davies, 2001; Rutqvist et al., 2002),

$$\varphi = \varphi_r + (\varphi_0 - \varphi_r)e^{-\alpha\sigma_e} \tag{4}$$

where φ_0 is the porosity at a reference effective stress (zero), φ_r is the porosity under higher effective stress conditions, σ_e represents the effective mean stress, Pa, and α is rock compressibility, Pa^{-1}.

Changes in matrix permeability may be related to the evolution of porosity using the classical Kozeny-Carman model (Nghiem et al., 2004),

$$k = k_0 \cdot \left(\frac{\varphi}{\varphi_0}\right)^3 \cdot \left(\frac{1-\varphi_0}{1-\varphi}\right)^2 \tag{5}$$

where k_0 and φ_0 are the initial permeability and porosity respectively.

2.2. Reservoir characteristics and model setup

2.2.1. Determination of storage space in abandoned mines

In longwall coal mines, for example, as the coal face advances, the overburden in the goaf deforms and collapses and eventually forms “three-zones” (Fig. 1a) during the mining operation. A caved zone fills with fragmented rock as a surrounding fracture zone generates numerous fractures with high permeability and porosity – and this can meet the requirements for fluid extraction and energy storage. Above the panel is a zone of subsiding strata that experiences minimal disturbance and lacks water storage capacity, typically consisting of lower permeability rocks – this zone acts as a caprock to the underlying reservoir. Accurately establishing a reservoir model for abandoned mine workings remains challenging due to the scarcity of data and extensive computational requirements (Rodríguez and Díaz, 2009). However, estimates based on empirical formulae can provide initial and effective evaluations of the energy storage system.

Heights H_c and H_f in the caved and fracture zones, may be recovered from empirical formulae as follows (Jiang et al., 2021),

$$H_c = \frac{100H_m}{c_1 H_m + c_2} \pm c \tag{6}$$

$$H_f = \frac{100H_m}{c_3 H_m + c_4} \pm c \tag{7}$$

where $c_1 \sim c_4$ and c are empirical parameters (Guo et al., 2018), H_m represents the coal seam thickness, m, and the reservoir height can be determined by calculating H_c and H_f, m.

An underground in-situ stress database for Chinese coal mines also summarizes regression equations for stress variation with depth as (Kang

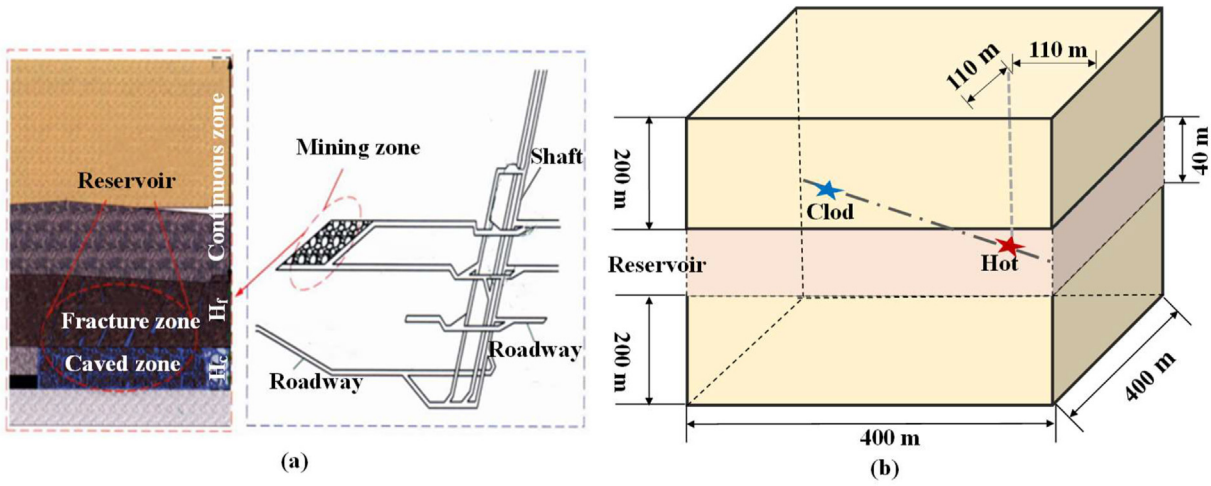

Fig. 1. (a) Structural geometry of an abandoned mine (Pu et al., 2022) and (b) simplified model of an abandoned mine "geothermal battery" energy storage system.

et al., 2019),

$$\sigma_v = 0.0245H \tag{8}$$

$$\sigma_H = 0.0215H + 3.267 \tag{9}$$

$$\sigma_h = 0.0113H + 1.954 \tag{10}$$

where σ_v, σ_H, σ_h represent vertical stress, maximum horizontal principal stress and minimum horizontal principal stress, MPa, and H represents depth, m.

2.2.2. Model setup

A numerical model representing a typical working face and goaf was established using an equivalent porosity simplification method for analysis (Fig. 1b). The model is based on the following assumptions: (1) the reservoir is in a quasi-stable state after a long period of overburden compaction, and under homogeneous geological conditions (Rodríguez and Díaz, 2009). (2) The height of the coal seam available for extraction is 3 m (Pruess and Bodvarsson, 1984). The height of the fractured reservoir, based on the empirical formulae of (7) and (8), is taken at 40 m. (3) Typical working face dimensions for abandoned mine goafs (Cun et al., 2021) are set at 400 m × 400 m × 40 m. (4) An injection well for hot water is located 110 m away from the model boundary (Fig. 1b indicated by a red pentagram) with a recovery well an identical distance from the boundary across the diagonal of the schematic model (Fig. 1b indicated by a blue pentagram). The initial reservoir temperature is 50 °C at a depth of 1000 m for an average geothermal gradient of 0.025 °C·m^{-1}. Initial pressure is set to 8 MPa with initial boundary stresses along the remote x, y, and z-direction assigned at 12 MPa, 12 MPa, and 20 MPa, and with no-flow boundary conditions applied. A schematic model for this study is established as shown in Fig. 2 with basic model parameters listed in Table 1.

2.2.3. Injection and extraction scenarios

The injection and extraction strategy involve the daily injection of solar-heated water through the hot well (Fig. 1b "hot") at a constant rate for 8 h (Green et al., 2021). Then, the hot water is extracted from the hot well at the same rate. Simultaneously, the cold well (Fig. 1b "cold") extracts or injects water at the same rate to maintain a balance in reservoir pressure, preventing excessive pressure changes that could result in reservoir subsidence or caprock fracturing. After the injection and extraction process is completed, the cold and hot wells are then shut-off. A new injection-extraction cycle then begins 8 h later. Figure 3 illustrates

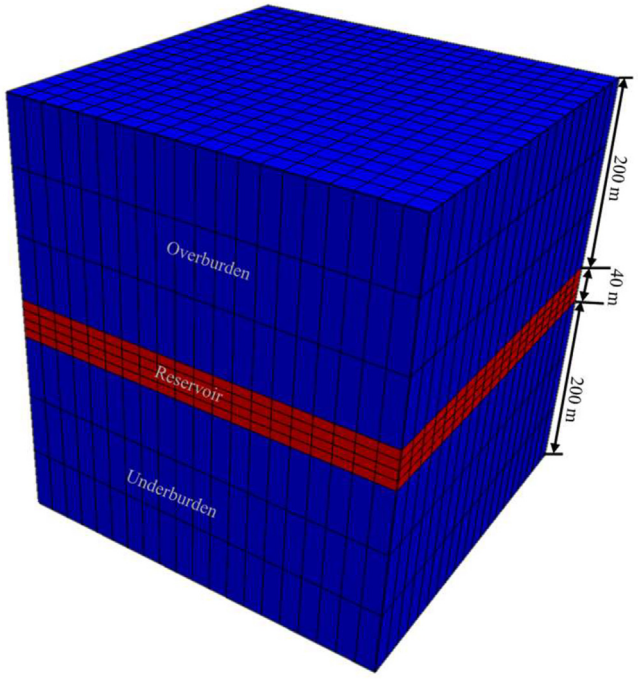

Fig. 2. The geothermal battery energy storage system model established using FLAC^{3D}-TOUGH2.

Table 1
Basic parameters for a geothermal battery energy storage system model (Green et al., 2021; Guo et al., 2023; Sirdesai et al., 2019; Zhang and Zhang, 2019)

Parameters	Reservoir	Overburden/ Underburden
Rock density (kg/m^3)	2000	2500
Initial permeability (×10^{-15}m^2)	1000	0.01
Initial porosity	0.25	0.025
Initial Pressure (MPa)	8	8
Formation thickness (m)	40	200
Specific heat of rock (J/(kg°C))	918	770
Thermal Conductivity (W/(m^{2}K))	2.51	1.05
Thermal expansion (°C^{-1})	3 × 10^{-5}	
Geothermal gradient (°C·m^{-1})	0.025	
Specific heat capacity of water (J/(kg·°C))	4200	

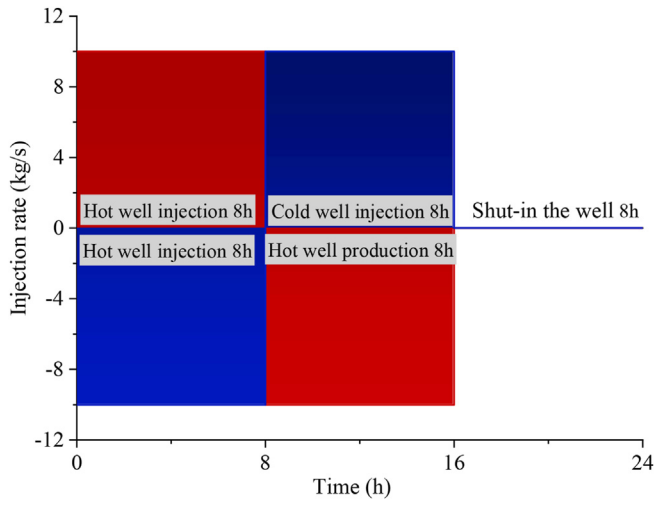

Fig. 3. Operating mode of the injection and extraction cycle (using 10 kg/s as an example).

the working mode of a cold and hot well during an injection-extraction cycle (using an injection rate of 10 kg/s as an example).

Concentrated solar power (CSP) technology uses lenses, emitters, and other devices to concentrate solar energy and convert it into thermal energy. The main forms of CSP include parabolic trough collectors, parabolic dish collectors, central tower receivers, and linear Fresnel reflectors. The operating temperatures of these systems generally range between 250 °C and 400 °C (Kincaid et al., 2018). So, when considering the effect of injection temperature on the reservoir, the injection temperature was changed to 50 °C, 100 °C, 150 °C, 200 °C, 250 °C, while keeping the injection rate at 10 kg/s. When assessing the impact of injection rate on the reservoir deformation, the injection temperature was kept at 250 °C and the injection rates was changed to 1 kg/s, 5 kg/s, 10 kg/s, as indicated in Table 2. The results are compared with a homogeneous and isotropic horizontal permeability model.

3. Results

3.1. Different injection temperature

3.1.1. Permeability and porosity evolution of reservoir

The injection of hot water leads to an increase in reservoir temperature. Figure 4a presented the evolution of rock temperature at the injector monitoring point. However, due to the heat exchange between the injected hot water and the initially cooler reservoir, there is significant initial heat loss during the early injection cycles, until a thermal equilibrium state is established after multiple cycles. The higher injection temperature leads to greater rock thermal energy build-up, and also with larger fluctuations during the cycles. Furthermore, both reservoir permeability and porosity decrease as the temperature rises during the injection phase, with higher injection temperatures leading to more significant reductions in permeability and porosity. For instance, the permeability loss is approximately 1×10^{-13} m^2 at an injection temperature of 250 °C (Fig. 4b). During the extraction phase, there is a slight decrease in rock temperature, resulting in a minor recovery in both permeability and porosity. This observation indicated a thermal damage to the formation connectivity, resulting from the heat exchange process from the hot fluids to the rock formation. Also, the formation damage is positive correlated with the temperature of injected fluids.

Table 2
Injection and extraction scenarios.

Case	Injection/Production temperature (°C)	Injection/Production rate (kg/s)
1	50	10
2	100	10
3	150	10
4	200	10
5	250	10
6	250	1
7	250	5
8	250	10

Figure 5 shows the variation in reservoir pore pressure throughout the injection and extraction cycles. During the injection phase, pore pressure increases, then decreases during the extraction phase. In the shut-in phase, pore pressure gradually returns to its initial state. When the injection temperature is 50 °C, which is equal to the reservoir temperature, the reservoir temperature remains unchanged throughout the injection-extraction cycles without the influence of thermal stress. Figure 4b' and 4c' demonstrate that both permeability and porosity increase during the injection phase, decrease during the extraction phase, and then return to their initial values during the shut-in phase. This behavior is consistent with the pressure changes at 50 °C injection temperature (Fig. 5). When the injection temperature exceeds the initial reservoir temperature, the high-temperature water generates thermal stresses due to the significant temperature difference within the relatively colder reservoir environment. The rock undergoes thermal expansion and compresses the existing pore space. The effect of pore fluid pressurization and induced thermal expansion acting on the reservoir result in a competition in the evolving the magnitude of permeability and porosity. The thermal stress plays a more significant role with higher injection temperatures – and minor role at lower temperatures. As shown in Fig. 4b and c, during each injection-extraction cycle, the impact on permeability and porosity becomes more pronounced with increasing injection temperature.

The magnitude of pressure fluctuation during the cycles of injection and extraction are also influenced by the injected fluid temperature. Pore pressure rises during the injection phase, decreases during the extraction phase and recovers to its initial pressure during the shut-in phase (Fig. 5). When the injection temperature is 50 °C, the range of pressure change is consistent for each injection-extraction cycle, and the pressure returns to its initial state during the shut-in phase. The reservoir permeability decreases under the influence of thermal stress when the injection temperature is higher than the initial reservoir temperature. Consequently, the fluctuation in the pressure during the injection-extraction cycles is greater when the injection temperature is $>$ 50 °C. During injection-extraction cycles, the pressure cycles between ~8.4 MPa (injection) and ~7.4 MPa (extraction) and returns to 8.2 MPa in the 30th cycle at $T = 250$ °C. With an increased injection temperature, the maximum pore pressure ~9 MPa, due to the most pronounced thermal stress.

3.1.2. Reservoir deformation response

The magnitude of the induced thermal stress is directly controlled by the injection rate and temperature, which also defines the potential for rock deformation (Uribe-Patiño et al., 2017). Figure 6 presents the dynamic changes in reservoir volumetric strain near the hot well during 30 injection-extraction cycles at different injection temperatures. Within each cycle, the volume strain increases due to thermal expansion during the injection of hot water and decreases during extraction due to shrinkage. The decrement in volumetric strain from shrinkage during extraction is smaller than the increment of volumetric strain during injection. During the production stage, the pressure near the hot well is lower than in the surrounding region. As a result, cooler fluids from the surrounding region flows towards the low-pressure zone near the hot wellbore. This influx of cooler fluids causes a decrease in temperature which leads to a slight recovery in rock deformation and a reduction in volumetric strain. Overall, the volumetric strain in the reservoir is directly proportional to the number of injection and extraction cycles, and increases with the increasing number of cycles, as supported by the dynamic evolution of reservoir rock temperature shown in Fig. 4a.

Figure 7 shows the porosity distribution in the reservoir after the

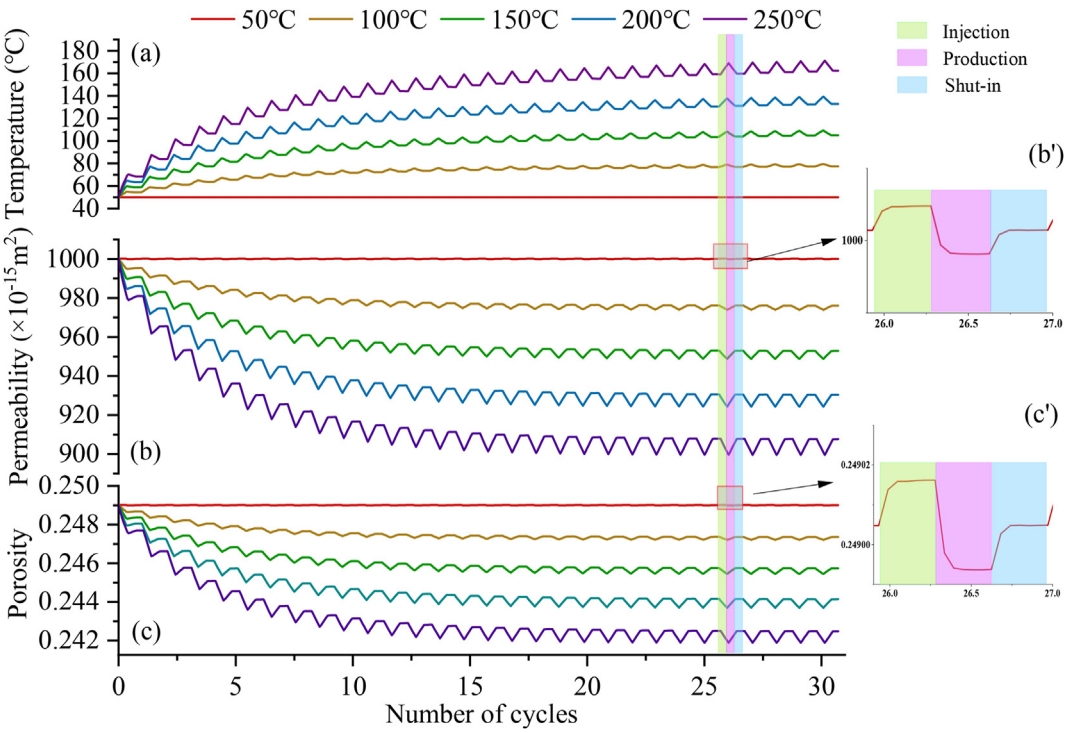

Fig. 4. Dynamic evolution of reservoir (a) temperature, (b) permeability, (c) porosity during injection and extraction cycles at different injection temperatures, (b′) permeability change in one cycle at 50 injection temperature and (c′) porosity change in one cycle at 50 °C injection temperature.

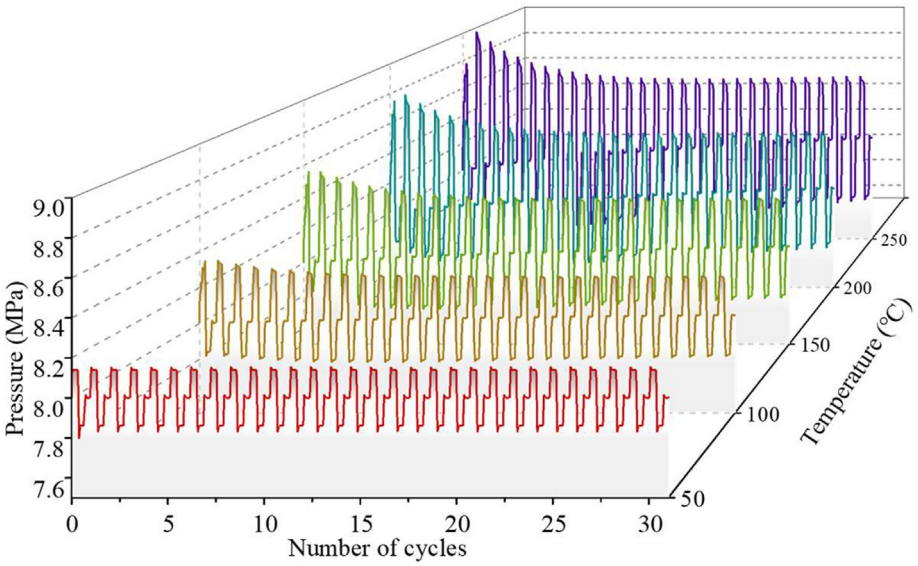

Fig. 5. Dynamic evolution of reservoir pore pressure at different injection-extraction temperatures.

6th, 18th and 30th cycles at different temperatures. Higher injection temperatures result in greater compression of the reservoir pore space at the same number of injection-production cycles. A decrease in volumetric deformation indicated porosity reduction. The spatial distribution of volume strain near the hot well (Fig. 8) shows that regions with higher temperatures respond with greater volume strain. As the number of injection-production cycles increases, porosity damage becomes more severe and volume deformation progressively intensifies with a constant injection temperature, causing noticeable deformation in the overburden and underburden by the end of the 30th injection-production cycle – especially at high temperatures of $T = 200$ °C and $T = 250$ °C (Fig. 8). The deformation of the caprocks directly impacts the sealing of the energy storage system.

3.2. Different injection rates

3.2.1. Permeability and porosity evolution of reservoir

Figure 9 depicts the evolution of reservoir temperature, permeability, and porosity at various injection rates. A higher injection rate leads to the reservoir temperature stabilizing more rapidly, requiring fewer cycles to reach the thermal equilibrium. This is because the higher injection rate results in the reservoir absorbing more heat energy within the same injection cycles, causing a more rapid increase in temperature. In particular, the reservoir temperature begins to stabilize after ~15 cycles when

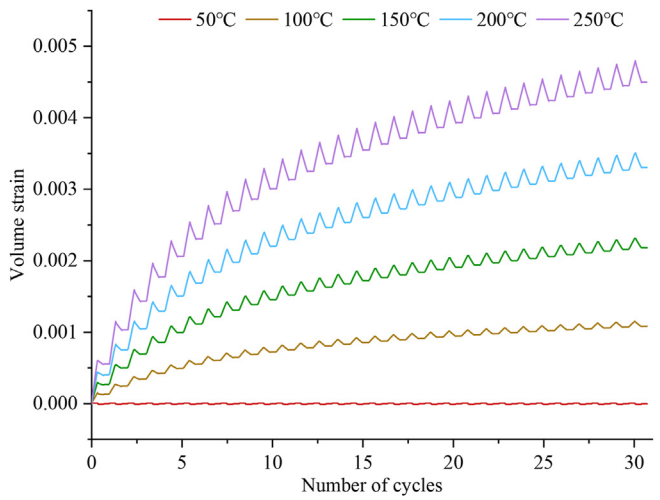

Fig. 6. Dynamic evolution of reservoir volumetric strain near the hot well at different temperatures.

the rate is 10 kg/s. However, the reservoir temperature continues to increase significantly even after 30 cycles when the rate is 1 kg/s, suggesting that it may take longer to reach a stable state at the lower injection rate. Reservoir permeability and porosity decrease with an increase in temperature during the injection-production cycles (Fig. 9b and a). This trend of decreasing permeability and porosity with increasing temperature is consistent with the observed trend in temperature at each injection rate. Higher injection rates require fewer cycles to reach a dynamic equilibrium of porosity and permeability. At an injection rate of 10 kg/s, porosity and permeability stabilize after ~15 cycles. These values are close to dynamic equilibrium after the 22nd cycle at 5 kg/s but are still not equilibrated after 30 cycles at a rate of 1 kg/s. Thus, identifying the need for a longer equilibration stage at lower injection rates.

Figure 10 provides a dynamic view of how reservoir pore pressure evolves at various injection rates. When the injection rate is lower, the reservoir experiences reduced fluctuations in pressure during the injection and production processes. The pressure difference between the injection and production phases is ~0.15 MPa when the rate is 1 kg/s. In essence, a lower injection rate translates to reduced pressure change within the reservoir, which enhances both the stability and safety for the energy storage system. In practical applications, it is essential to determine the optimal injection and production strategy based on the specific reservoir conditions to ensure a balance between safety and efficiency.

3.2.2. *Reservoir deformation response*

Figure 11 illustrates the dynamic evolution of reservoir volumetric strain near the hot well across various injection rates. A higher injection rate corresponds to a larger volumetric strain. Increased injection rate results in a larger volume of hot water and thus heat during each injection cycle, further elevating the temperature of the rock. Consequently, this results in a greater volumetric strain within the reservoir due to the expansion of the rock.

Figure 12 depicts the spatial distributions of reservoir porosity and volumetric strain near the injection well at the end of the 6th, 18th, and 30th cycles and for various injection rates. At the same injection rate, the expansion of the rock increases as the number of cycles grow, resulting in more significant volumetric strain. During a single injection cycle, a higher injection rate leads to a more substantial temperature increase (Fig. 9a) and increased deformation within the reservoir. The impact on caprock expansion is not as significant as that in the reservoir, especially for the caprock above the hot well. When the reservoir volumetric strain reaches a certain threshold, the deformation of the caprocks becomes highly noticeable. After 30 cycles, the volumetric strain approaches 0.005 for an injection rate of 10 kg/s (Fig. 11) and significant deformation of the caprocks can be observed across a broad area (Fig. 12a).

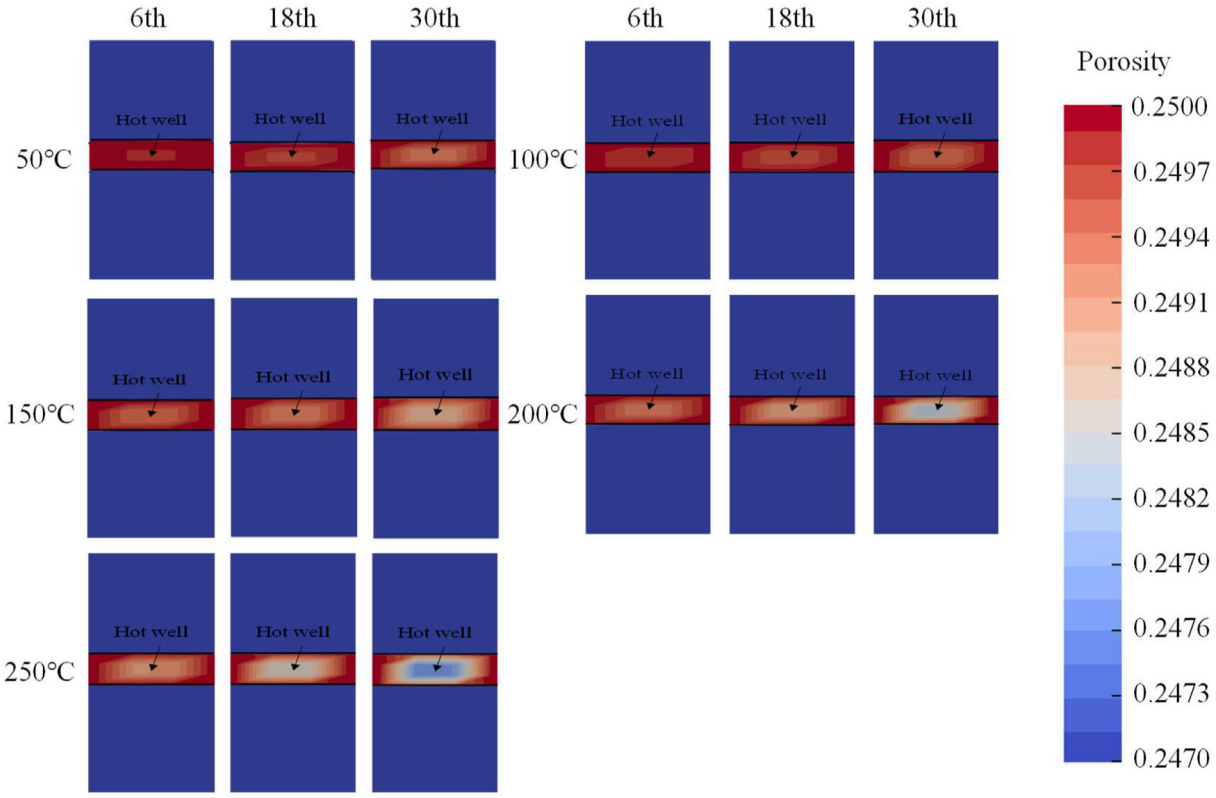

Fig. 7. Spatial distribution maps of reservoir porosity near the hot well at the end of the 6th, 18th, and 30th cycles for different temperatures.

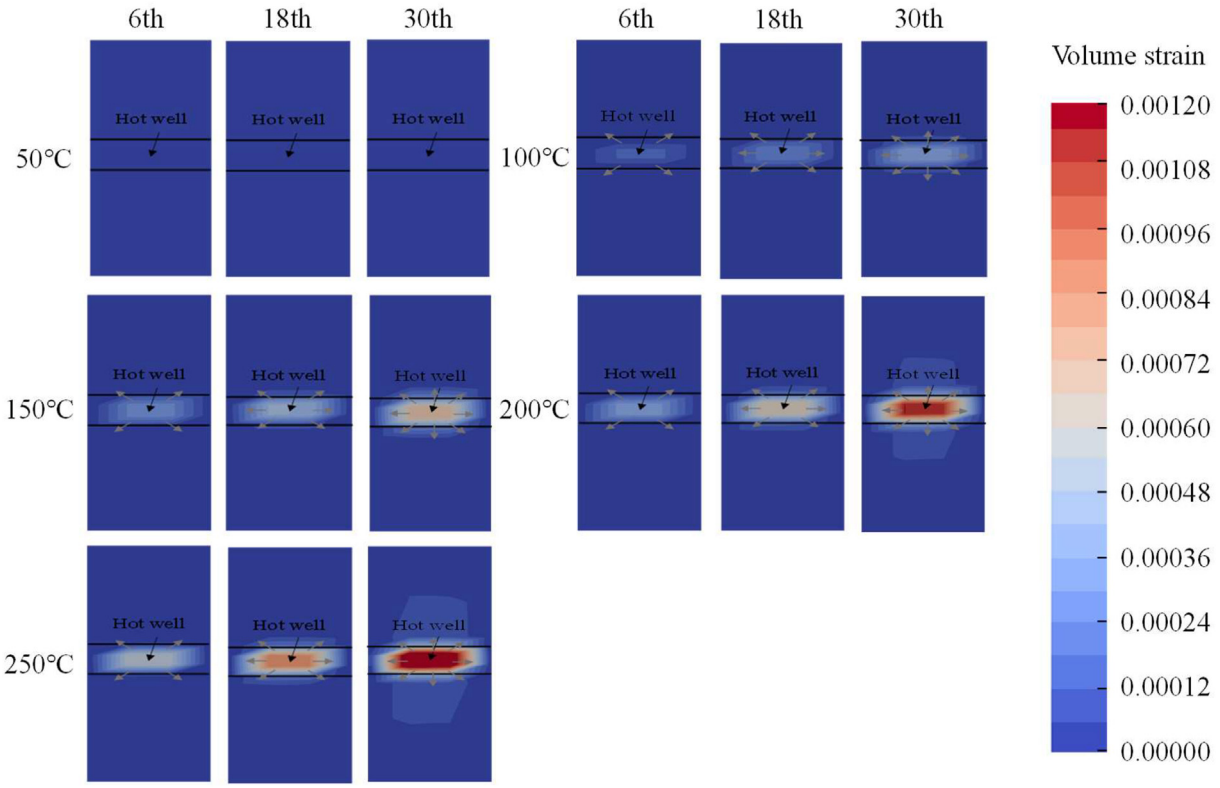

Fig. 8. Spatial distribution of reservoir volumetric strain near the hot well at the end of the 6th, 18th, and 30th cycles for different temperatures.

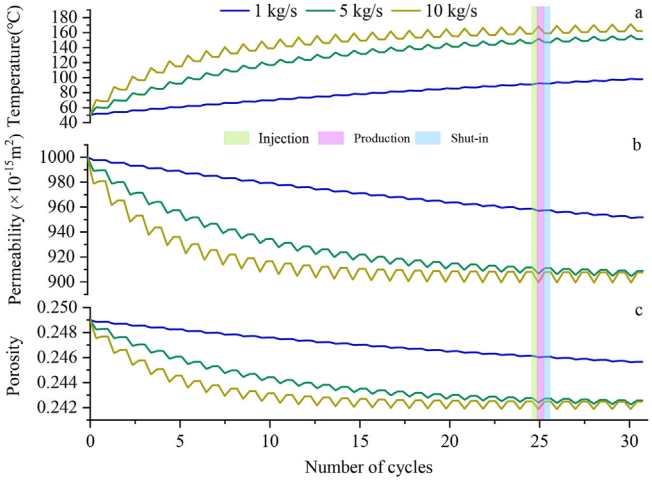

Fig. 9. Dynamic evolution of reservoir (a) temperature, (b) permeability, and (c) porosity during injection and extraction cycles at different injection-extraction rates.

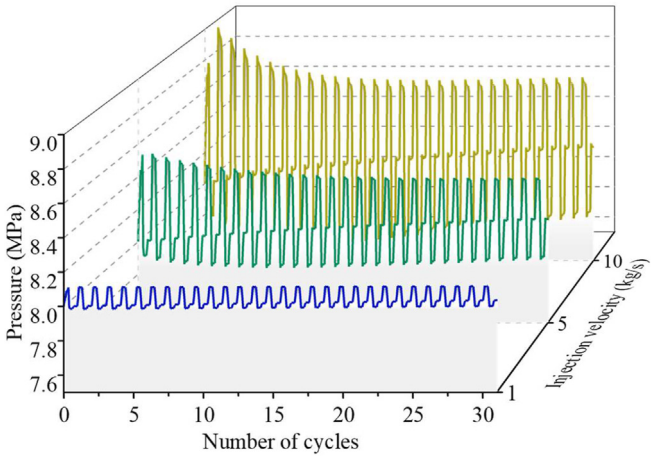

Fig. 10. Dynamic evolution of reservoir pore pressure at different injection-extraction rates.

3.3. Monitoring of overburden and underburden displacements

Displacements within the caprock vary radially outwards from the injection well. Figure 13a shows the locations of eight displacement monitoring points in the caprock, distributed between the injection well and the production well. In Fig. 13b, the displacement of both the overburden and underburden is shown at different temperatures following 30 cycles of injection-production. These displacement measurements with different injection rates are on the order of millimeter scale – maximum at the well and decreasing radially outwards. The caprock effectively dampen the cyclic displacement caused by reservoir expansion through its largely isothermal compaction. As a result, the overburden formation experiences uplift, while the underburden sinks.

Higher-temperature hot water induces more substantial thermal stress, leading to greater reservoir expansion and subsequently larger displacements in the caprock (Fig. 13b). Moreover, a higher injection rate results in a larger displacement in the caprock (Fig. 13c). Displacement magnitudes decrease with proximity to the cold well, and the underburden displacements are null at ~60 m from the hot well. The distribution of displacements in the longitudinal direction also overlap with the distribution of the heating regime – indicating that induced thermal stresses affect the deformation. At 250 °C, the caprock experiences a maximum uplift displacement of ~7.5 mm, whereas the underburden subsides by −6 mm (Fig. 13b). The caprock exhibits a greater uplift compared to the subsidence of the bedrock under a consistent injection

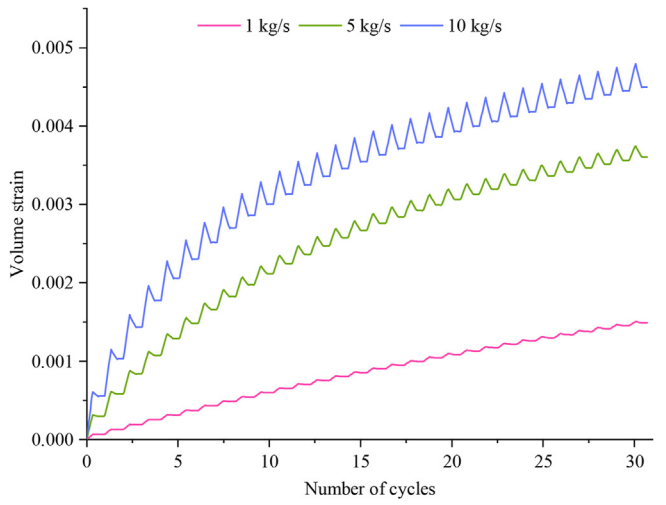

Fig. 11. Dynamic evolution of reservoir volumetric strain near the hot well for injection at different rates.

rate (Fig. 13c). This difference is attributed to the lack of constraint on the caprock provided by the free surface boundary. After 30 cycles of injection-production, the pressure is higher than the initial reservoir pressure, when the injection temperature surpasses 50 °C (Figs. 5 and 10) – due to thermal effects. During the shut-in phases, the pressure rapidly equilibrates and uniformly distributed throughout the entire reservoir. This results in a net increase in pressure across the entire reservoir and a reduction in effective stress, causing reservoir dilation and subsequent uplift at the overburden and underburden formations. Moreover, the displacement is primarily controlled by the boundary of heating zones, by comparing the distribution of temperature and displacement along the wells.

A vertical profile of four displacement monitoring points tracks displacements directly above the vertical hot well (Fig. 14a) – with the impacts of different temperature injection shown in Fig. 14b. As the temperature increases, the displacement within the overburden correspondingly increases, although vertical displacement decreases with increased vertical separation from the reservoir. The displacement for monitoring point #1 situated 220 m above the hot well is 1.53 mm as the temperature approaches 165 °C. Thus, no significant surface displacement will exist say ~1000 m above the thermal well after 30 cycles of injection-production.

Our inference is that the injected hot water heats the reservoir injection during cycles, causing deformation due to thermal stress within a relatively cooler environment. The thermal expansion resulting from continuous injection of hot fluids may also result in significant formation damage and reduction in in-situ permeability and porosity – this will also be proportional to the injected fluid temperature and rate. When the duration of the multiple injection-then-production cycles are sufficiently long (many cycles) the reservoir will reach a dynamic thermal equilibrium. In this state the entire system (reservoir-underburden-overburden) will be in dynamic equilibrium, forming an ideal "thermal storage cavity" in the vicinity of the hot well.

4. Discussion

The deformation of the reservoir during energy storage results from the combined effects of poroelasticity and thermal expansion (Li et al., 2023). As discussed in Section 3, the changes in pore pressure and temperature are the main factors impacting variations in permeability and porosity within the reservoir. The formation is initially in equilibrium under the original formation pressure with the injection of hot water subsequently elevating the pressure and heating the reservoir. The resulting thermal expansion creates a competitive between heating compacting the porosity and increased pressure dilating the reservoir. When the thermal stress generated by the rock exceeds the change in effective stress due to the elevated pore pressure then permeability will be reduced.

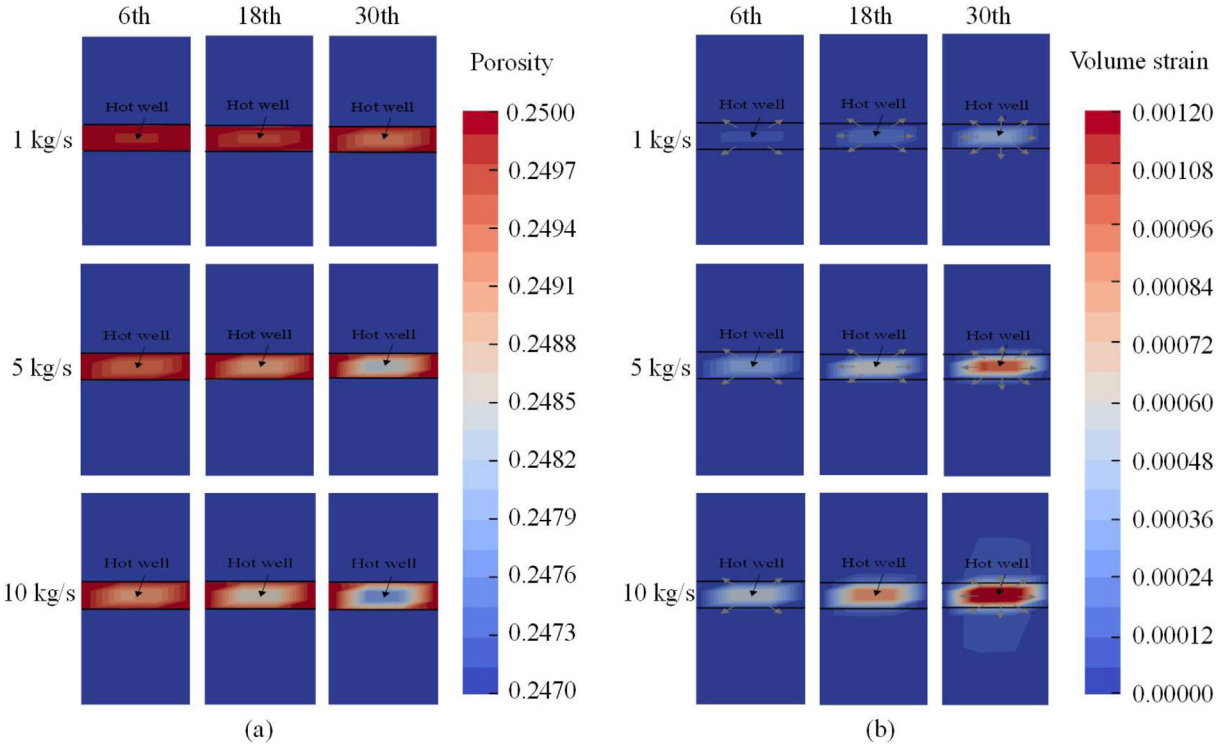

Fig. 12. Spatial distribution maps of reservoir (a) porosity and (b) volumetric strain near the hot well at the end of the 6th, 18th, and 30th cycles for different injection rates.

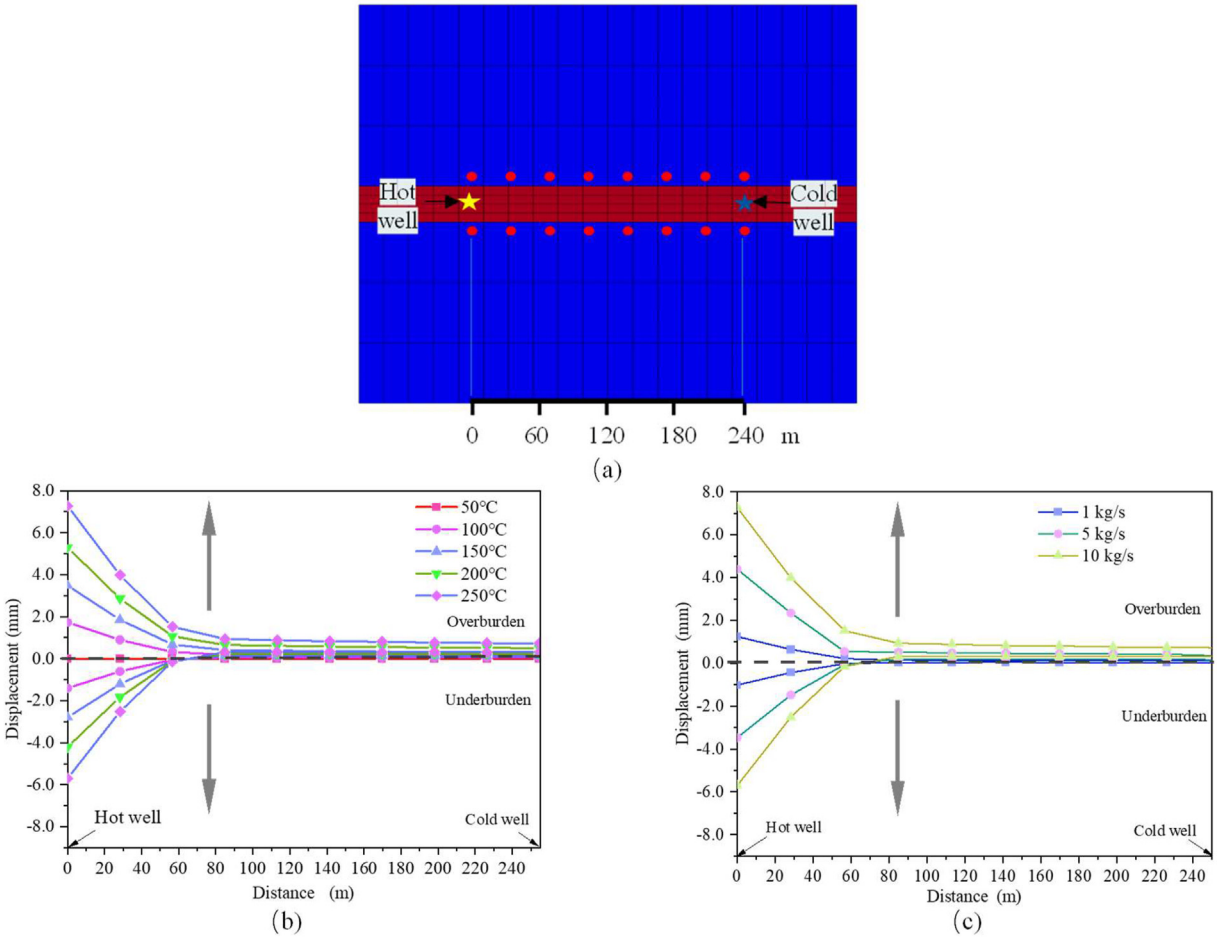

Fig. 13. (a) Distribution of the locations displacement monitoring points between the injection well and the production well, (b) displacement changes in the overburden and underburden for injection at different temperatures, (c) displacement changes in the overburden and underburden for injection at different rates.

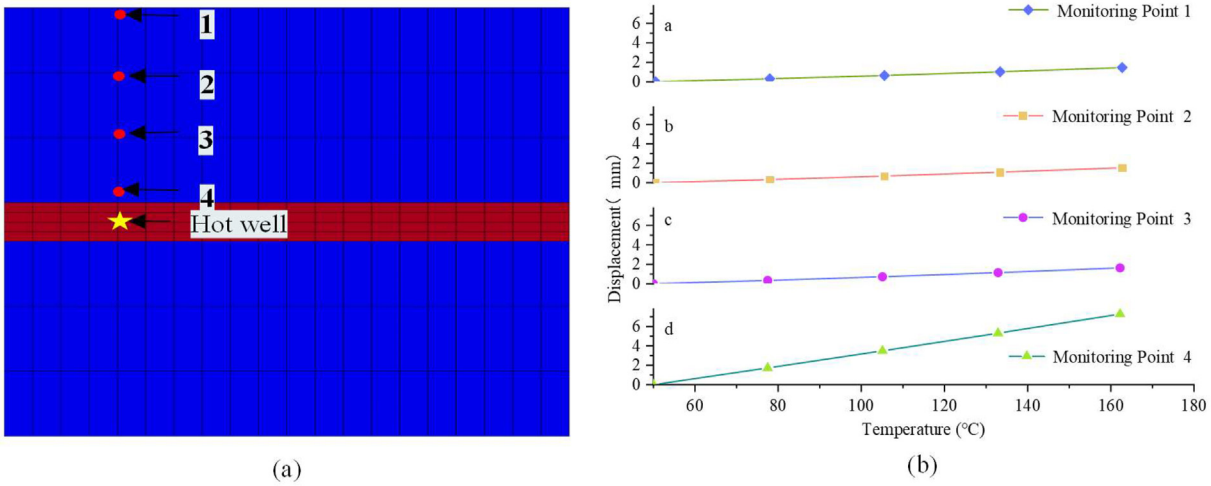

Fig. 14. (a) Profile of four displacement monitoring points above the vertical hot well, (b) displacement of the overburden above the vertical hot well with temperature increase.

In real geological formations, pores and microcracks serve as permeable flow channels and are sensitive to changes in effective stress (Pan et al., 2019; Huang et al., 2021). In these stress sensitive systems, the injection of hot water potentially reduces permeability by thermal expansion with the overpressures countering this effect (Meng et al., 2021). Figure 15 depicts the deformation mechanisms of multi-scale pores during injection then production cycles. In the initial phase, the interconnected pores within the reservoir provide an efficient pathway for fluid flow. Injection increases fluid pressure with thermal effects delayed by the thermal capacitance of the system (Zhang et al., 2021). Resulting in a delayed impact of the thermal effect causing a noticeable channel constriction (Xu et al., 2023). In some cases, this constriction

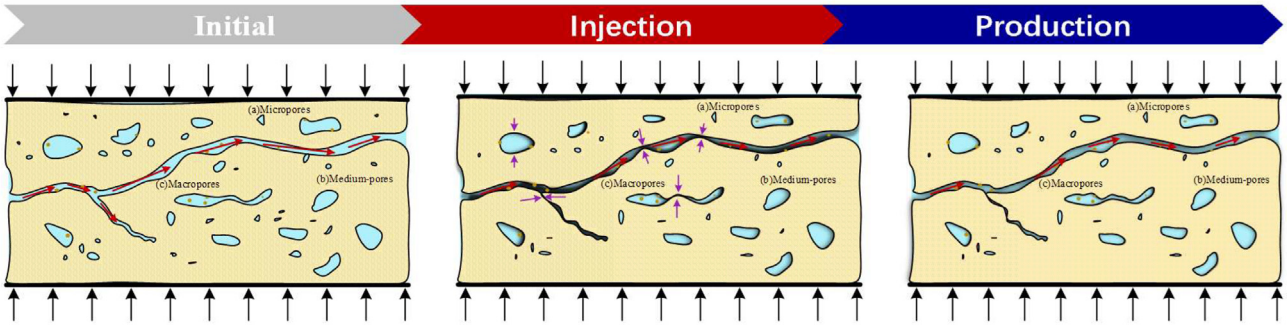

Fig. 15. Deformation mechanisms of multi-scale pores during the injection and production process.

may cause a transitioning from meso-pores to micro-pores, leading to a significant reduction in permeability. Meso-pores may lose connectivity with the surrounding small pores, and micropores may disappear due to the expansion and compression of the rock (Huang et al., 2021). During the production phase, the area around the hot well transitions into a low-pressure zone, with the influx of surrounding cold water contributing to a decrease in rock temperature (Figs. 4a and 9a), resulting in a minor dilation of the permeable flow channels. This dynamic evolution corresponds with the expansion observed in the reservoir volumetric strain presented in Figs. 6 and 11. Moreover, clay minerals may be present in the rock matrix and become mobilized in the flow – potentially occluding pores and reducing permeability (De Silva et al., 2017).

The magnitude of thermal stress is not solely contingent on the temperature change but also influenced by the coefficient of thermal expansion - which may vary among different mineral constituents comprising the reservoir (Roshan et al., 2015). Figure 16 shows the evolution of permeability and porosity within the reservoir different thermal expansion coefficients. As the thermal expansion coefficient of the reservoir rock increases, the reduction in permeability and porosity becomes more substantial. When the thermal expansion coefficient is set at $3 \times 10^{-5}\,^{\circ}C^{-1}$, the porosity decreases from the initial value of 0.25 to 0.242, resulting in a nearly 10% loss in permeability.

5. Conclusions

A sequentially coupled model (FLAC^{3D}-TOUGH2) was used to investigate the thermo-hydro-mechanical (THM) response of a reservoir to the injection of hot fluids for thermal storage as a geothermal battery. The evolution of permeability was tracked during diurnal cyclic injection-then-production over multiple cycles. This is used to explore the influence of injection-then-production rates and temperatures and reservoir rock thermal expansion coefficient on the evolution of reservoir porosity and permeability and performance of the system, including external deformations. The main conclusions are as follows.

(1) The principal mechanisms driving reservoir deformation result from the combined influence of poroelastic and thermal effects – and these effects are generally competitive. As the temperature in the reservoir increases, rock mineral particles are subjected to thermal expansion. When the thermal stress becomes predominant, reservoir volume expands as seepage channels are squeezed and narrowed and permeability decreases.

(2) Elevated injection temperatures increase the reduction in porosity and permeability within the reservoir and this effect dominates at high temperatures of the poromechanical impact of increased pressures. At an injection temperature of 250 °C, permeability is reduced by ~10%. Because the reservoir temperature is low in the pre-injection period, more heat is needed to heat it up, and the lower the injection temperature, the longer the period needed to heat up the reservoir to the target temperature.

(3) Deformation of the caprock is impacted by the volumetric strain of the reservoir and reflects reservoir displacements. The overburden displaces upwards directly above the reservoir with this displacement present to ~60 m from the well. At the reservoir temperatures close to 165 °C, the displacement of the rock 220 m above the hot well is 1.53 mm, and it is assumed that there will be no significant uplift on the surface after 30 injection-production cycles at reservoir depths of 1000 m.

The optimization of injection temperatures and rates is of paramount

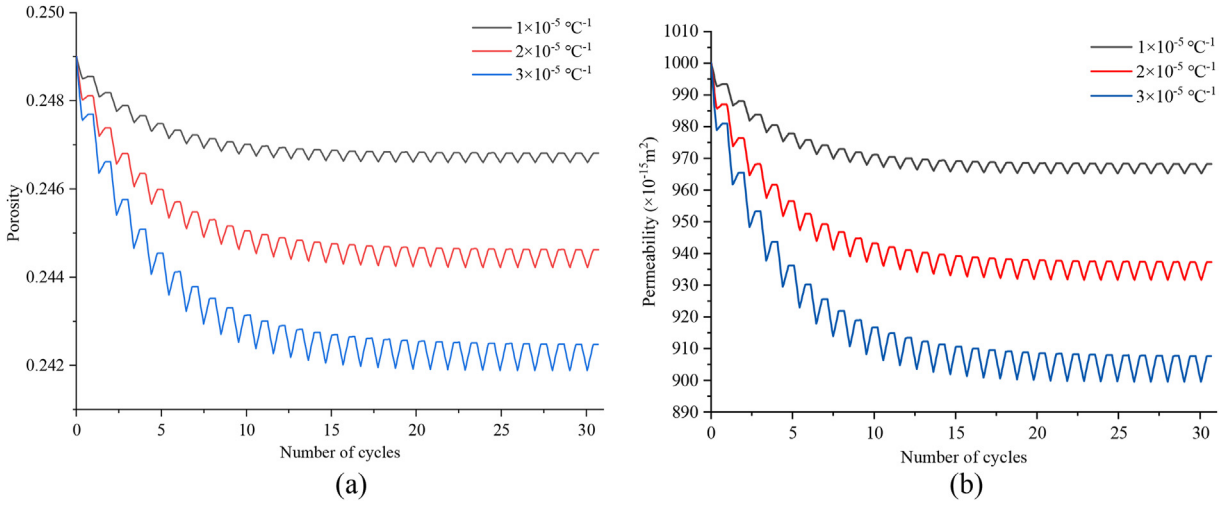

Fig. 16. Impact of different thermal expansion coefficients on reservoir (a) porosity and (b) permeability.

importance, particularly when considering geological conditions and the potential implications of these modifications on reservoir properties and the response of the overburden. The geothermal battery energy storage system is still in the conceptual stage. Current research is primarily based on an equivalent simplified processing model established by previous researchers' empirical values. There are discrepancies between simulation results and actual conditions. In the future, obtaining actual geological parameters and distribution of fractures can be used to establish a more accurate model for achieving precise predictions of surface uplift and energy storage efficiency.

CRediT authorship contribution statement

Yanting Liu: Writing – review & editing, Writing – original draft, Formal analysis, Data curation, Conceptualization. **Yuan Liang:** Resources. **Yueqiang Ma:** Resources. **Jingyi Liu:** Visualization. **Derek Elsworth:** Writing – review & editing. **Quan Gan:** Conceptualization.

Declaration of competing interest

The authors declare the following financial interests/personal relationships which may be considered as potential competing interests: Quan Gan reports financial support was provided by the National Key Research and Development Program of China. If there are other authors, they declare that they have no known competing financial interests or personal relationships that could have appeared to influence the work reported in this paper.

Acknowledgements

Funding for this research was received from the National Key Research and Development Program of China (Grant No. 2021YFC3000603) and the General Program of National Natural Science Foundation of China (Grant No. 5217041034). This work is also supported by Science & Technology Department of Sichuan Province (Grant No. 2022YFSY0008). DE gratefully acknowledges support from the G. Albert Shoemaker endowment.

References

Bartela, A., Ochmann, J., Waniczek, S., Lutyński, M., Smolnik, G., Rulik, S., 2022. Evaluation of the energy potential of an adiabatic compressed air energy storage system based on a novel thermal energy storage system in a post mining shaft. J. Energy Storage 54, 105282. https://doi.org/10.1016/j.est.2022.105282.

Becattini, V., Motmans, T., Zappone, A., Madonna, C., Haselbacher, A., Steinfeld, A., 2017. Experimental investigation of the thermal and mechanical stability of rocks for high-temperature thermal-energy storage. Appl. Energy 203, 373–389. https://doi.org/10.1016/j.apenergy.2017.06.025.

Blanco Martín, L., Wolters, R., Rutqvist, J., Lux, K., Birkholzer, J.T., 2015. Comparison of two simulators to investigate thermal–hydraulic–mechanical processes related to nuclear waste isolation in saliferous formations. Comput. Geotech. 66 (C), 219–229. https://doi.org/10.1016/j.compgeo.2015.01.021.

Cun, Z., Fangtian, W., Bai, Q., 2021. Underground space utilization of coalmines in China; A review of underground water reservoir construction. Tunn. Undergr. Space Technol. 107, 103657. https://doi.org/10.1016/j.tust.2020.103657.

Davies, J.P., Davies, D.K., 2001. Stress dependent permeability characcterization and modeling. SPE J. 2 (6), 224–235. https://doi.org/10.2118/71750-PA.

De Silva, G.P.D., Ranjith, P.G., Perera, M.S.A., Dai, Z.X., Yang, S.Q., 2017. An experimental evaluation of unique co2 flow behaviour in loosely held fine particles rich sandstone under deep reservoir conditions and influencing factors. Energy 119, 121–137. https://doi.org/10.1016/j.energy.2016.11.144.

Fang, H., Li, A., Sang, S., et al., 2023. Numerical analysis of permeability rebound and recovery evolution with thm multi-physical field models during cbm extraction in crushed soft coal with low permeability and its indicative significance to co2 geological sequestration. Energy 262, 125395. https://doi.org/10.1016/j.energy.2022.125395.

Gan, Q., Elsworth, D., Zhao, Y., Grippa, A., Hurst, A., 2020. Coupled hydro-mechanical evolution of fracture permeability in sand injectite intrusions. J Rock Mech Geotech 12 (4), 742–751. https://doi.org/10.1016/j.jrmge.2019.10.007.

Green, S., Mclennan, J., Panja, P., Kitz, K., Allis, R., Moore, J., 2021. Geothermal battery energy storage. Renew. Energy 164, 777–790. https://doi.org/10.1016/j.renene.2020.09.083.

Guo, P., Wang, M., Dang, G., Zhu, T., Wang, J., He, M., 2023. Evaluation method of underground water storage space and thermal reservoir model in abandoned mine. Rock Mechanics Bulletin 2 (2), 100044. https://doi.org/10.1016/j.rockmb.2023.100044.

Guo, T., Zhang, Y., Zhang, W., et al., 2022. Numerical simulation of geothermal energy productivity considering the evolution of permeability in various fractures. Appl. Therm. Eng. 201, 117756. https://doi.org/10.1016/j.applthermaleng.2021.117756.

Guo, P., Zheng, L., Sun, X., He, M., Wang, Y., Shang, J., 2018. Sustainability evaluation model of geothermal resources in abandoned coal mine. Appl. Therm. Eng. 144, 804–811. https://doi.org/10.1016/j.applthermaleng.2018.06.070.

Hu, Y., Gan, Q., Hurst, A., Elsworth, D., 2018. Evolution of permeability in sand injectite systems. Int J Rock Mech Min 106, 176–189. https://doi.org/10.1016/j.ijrmms.2018.04.018.

Huang, Y., Yang, S., Teng, S., 2021. Temperature dependence of the permeability of sandstone under loading and unloading conditions of confining pressure. Math. Geosci. 53 (4), 551–570. https://doi.org/10.1007/s11004-020-09860-7.

Jello, J., Khan, M., Malkewicz, N., Whittaker, S., Baser, T., 2022. Advanced geothermal energy storage systems by repurposing existing oil and gas wells: a full-scale experimental and numerical investigation. Renew. Energy 199, 852–865. https://doi.org/10.1016/j.renene.2022.07.145.

Jiang, D., Chen, S., Liu, W., Ren, Y., Guo, P., Li, Z., 2021. Underground hydro-pumped energy storage using coal mine goafs: system performance analysis and a case study for China. Front. Earth Sci. 9. https://doi.org/10.3389/feart.2021.760464.

Josiane, J., Asce, S.M., Tugce, B., Ph, D.M.A., 2023. A fully coupled thermo-ahydro-mechanical response of an advanced geothermal energy storage system in a sedimentary basin. In: Geo-Congress on Sustainable Infrastructure Solutions from the Ground up, pp. 105–115. https://doi.org/10.3390/jmse11040766. Los Angeles, CA.

Kang, H., Yi, B., Gao, F., Lu, H., 2019. Database and characteristics of underground in-situ stress distribution in Chinese coal mines. J. China Coal Soc. 44 (1), 23–33. https://doi.org/10.13225/j.cnki.jccs.2018.5032.

Koohi-Fayegh, S., Rosen, M.A., 2020. A review of energy storage types, applications and recent developments. J. Energy Storage 27, 101047. https://doi.org/10.1016/j.est.2019.101047.

Kozhevnikov, E., Riabokon, E., Turbakov, M., 2021. A model of reservoir permeability evolution during oil production. Energies 14 (9), 2695. https://doi.org/10.3390/en14092695.

Li, G., Li, G., Luo, C., Zhou, R., Zhou, J., Yang, J., 2023. Dynamic evolution of shale permeability under coupled temperature and effective stress conditions. Energy 266, 126320. https://doi.org/10.1016/j.energy.2022.126320.

Liu, X., Lu, W., Li, M., Zeng, N., Li, T., 2020. The thermal effect on the physical properties and corresponding permeability evolution of the heat-treated sandstones. Geofluids 2020, 1–16. https://doi.org/10.1155/2020/8838325.

Meng, T., Li, E., Xue, Y., Ma, J., Liu, W., Xufeng, L., 2021. Experimental study on permeability and porosity evolution of host rock with varying damage degrees in excavation damaged area under real-time ultra-high temperature and triaxial stress/seepage pressure condition. Bull. Eng. Geol. Environ. 80 (10), 8075–8097. https://doi.org/10.1007/s10064-021-02408-x.

Nghiem, L., Sammon, P., Grabenstetter, J., Ohkuma, H., 2004. Modeling co_2 Storage in Aquifers with a Fully-Coupled Geochemical Eos Compositional Simulator. Society of Petroleum Engineers. https://www.researchgate.net/publication/238049854.

Panja, P., Mclennan, J., Green, S., 2021a. Influence of permeability anisotropy and layering on geothermal battery energy storage. Geothermics 90, 101998. https://doi.org/10.1016/j.geothermics.2020.101998.

Pan, J., Zhang, Z., Li, M., Wu, Y., Wang, K., 2019. Characteristics of multi-scale pore structure of coal and its influence on permeability. Nat. Gas. Ind. B 6 (4), 357–365. https://doi.org/10.1016/j.ngib.2019.01.012.

Ping, L., Lai, Z., Sen, C., et al., 2020. Main challenges of closed/abandoned coal mine resource utilization in China. Energy Sources, Part A Recovery, Util. Environ. Eff. 42 (22), 2822–2830. https://doi.org/10.1080/15567036.2019.1618992.

Pruess, K., Bodvarsson, G.S., 1984. Thermal effects of reinjection in geothermal reservoirs with major vertical fractures. J. Petrol. Technol. 36 (10), 1567–1578. https://doi.org/10.2118/12099-PA.

Pruess, K., 2004. The tough codes-a family of simulation tools for multiphase flow and transport processes in permeable media. Vadose Zone J. 3 (3), 738–746. https://doi.org/10.2113/3.3.738.

Pu, H., Xu, J., Bian, Z., Holger, S., 2022. Research status and progress of geothermal energy development and utilization from closed/abandoned coal mines. J. China Coal Soc. 47 (6), 2243–2269. https://doi.org/10.13225/j.cnki.jccs.FQ21.1929.

Rodríguez, R., Díaz, M.B., 2009. Analysis of the utilization of mine galleries as geothermal heat exchangers by means a semi-empirical prediction method. Renew. Energy 34 (7), 1716–1725. https://doi.org/10.1016/j.renene.2008.12.036.

Roshan, H., Andersen, M.S., Acworth, R.I., 2015. Effect of solid–fluid thermal expansion on thermo-osmotic tests: an experimental and analytical study. J. Petrol. Sci. Eng. 126, 222–230. https://doi.org/10.1016/j.petrol.2014.12.005.

Rosenbrand, E., Kjøller, C., Riis, J.F., Kets, F., Fabricius, I.L., 2015. Different effects of temperature and salinity on permeability reduction by fines migration in berea sandstone. Geothermics 53, 225–235. https://doi.org/10.1016/j.geothermics.2014.06.004.

Rutqvist, J., Wu, Y.S., Tsang, C.F., Bodvarsson, G., 2002. A modeling approach for analysis of coupled multiphase fluid flow, heat transfer, and deformation in fractured porous rock. Int J Rock Mech Min 39 (4), 429–442. https://doi.org/10.1016/S1365-1609(02)00022-9.

Shao, J., You, L., Kang, Y., et al., 2020. Experimental study on stress sensitivity of underground gas storage. J. Petrol. Sci. Eng. 195, 107577. https://doi.org/10.1016/j.petrol.2020.107577.

Sirdesai, N.N., Mahanta, B., Ranjith, P.G., Singh, T.N., 2019. Effects of thermal treatment on physico-morphological properties of indian fine-grained sandstone. Bull. Eng. Geol. Environ. 78 (2), 883–897. https://doi.org/10.1007/s10064-017-1149-6.

Siratovich, P.A., von Aulock, F.W., Lavallée, Y., Cole, J.W., Kennedy, B.M., Villeneuve, M.C., 2015. Thermoelastic properties of the rotokawa andesite: a geothermal reservoir constraint. J. Volcanol. Geoth. Res. 301, 1–13. https://doi.org/10.1016/j.jvolgeores.2015.05.003.

Uribe-Patiño, J.A., Alzate-Espinosa, G.A., Arbeláez-Londoño, A., 2017. Geomechanical aspects of reservoir thermal alteration: a literature review. J. Petrol. Sci. Eng. 152, 250–266. https://doi.org/10.1016/j.petrol.2017.03.012.

Wang, T., Chang, J., Wang, H., 2023. A study of the deformation law of the surrounding rock of a laminated roadway based on flac3d secondary development. Appl. Sci. 13 (10), 6077. https://doi.org/10.3390/app13106077.

Wu, X., Li, P., Guo, Q., Cai, M., Ren, F., Zhang, J., 2022. Research progress on the evolution of physical and mechanical properties of thermally damaged rock. Chinese Journal of Engineering 44 (5), 827–839. https://doi.org/10.13374/j.issn2095-9389.2020.12.23.007.

Xu, Y., Xiao, J., Li, X., Xia, K., Peng, J., 2023. Experimental study on the permeability evolution of argillaceous sandstone under elevated temperatures. Eng. Geol. 313, 106974. https://doi.org/10.1016/j.enggeo.2022.106974.

Yang, S., Xu, P., Li, Y., Huang, Y., 2017. Experimental investigation on triaxial mechanical and permeability behavior of sandstone after exposure to different high temperature treatments. Geothermics 69, 93–109. https://doi.org/10.1016/j.geothermics.2017.04.009.

Zhang, Y., Zhao, G., 2023. A multiphysics method for long-term deformation analysis of reservoir rock considering thermal damage in deep geothermal engineering. Renew. Energy 204, 432–448. https://doi.org/10.1016/j.renene.2023.01.026.

Zhang, L., Huang, M., Xue, J., Li, M., Li, J., 2021. Repetitive mining stress and pore pressure effects on permeability and pore pressure sensitivity of bituminous coal. Nat. Resour. Res. 30 (6), 4457–4476. https://doi.org/10.1007/s11053-021-09902-9.

Zhang, C., Zhang, L., 2019. Permeability characteristics of broken coal and rock under cyclic loading and unloading. Nat. Resour. Res. 28 (3), 1055–1069. https://doi.org/10.1007/s11053-018-9436-x.